Optical transitions in PbTe/CdTe quantum dots

T. N. Xu, H. Z. Wu,* and J. X. Si

Department of Physics, Zhejiang University, Hangzhou, Zhejiang 310027, People's Republic of China

P. J. McCann

School of Electrical and Computer Engineering, Oklahoma University, Norman, Oklahoma 73019-1023, USA

Recently, intense room-temperature midinfrared luminescent emission has been observed in high-symmetry PbTe quantum dots (QDs) embedded in a (001)-oriented CdTe single crystalline matrix [W. Heiss *et al.*, Appl. Phys. Lett. **88**, 192109 (2006)]. To interpret the optical transition in these newly realized QDs, we have developed a four-band $\vec{k}\cdot\vec{p}$ model that takes into account the anisotropic effects of the band structure and finite-confinement potential in the QDs. The high order term $o(k_i^4)$ in the Hamiltonian is calculated using perturbation approximation methods. The simulation of the spontaneous emission of PbTe/CdTe QDs shows that two types of quantum structures were formed by the thermal annealing of the PbTe/CdTe quantum wells, as reported by Heiss *et al.*, and the calculations are in good agreement with the experimental observations of the dot sizes and photoluminescence. The model can be extended to the description of interband optical transitions in other IV-VI QDs, such as PbSe/PbTe and PbSe/PbEuTe QDs that usually have a large size (with a typical lateral size of 50 nm and height of 20 nm) and small quantum confinement potential ($<$100 meV) and are oriented in different directions.

PACS number(s): 78.55.−m, 78.20.Bh, 78.67.Hc, 78.30.−j

I. INTRODUCTION

Semiconductor quantum dots (QDs) have attracted much attention in the past few years due to their intrinsic physical nature and potential applications in a number of improved and novel electro-optical devices.[1] IV-VI semiconductors (such as PbTe, PbSe, and PbS) have several characteristics sufficiently different from more commonly studied III-V and II-VI semiconductors to justify further experimental and theoretical investigation. These characteristics include a symmetric conduction- and valence-band structure, a high dielectric constant, and a fourfold degenerate (neglecting spin) direct band gap at the L point in k space. Symmetric bands and high dielectric constants result in good confinement for both electrons and holes in low-dimensional structures. The Bohr radii for electrons and holes in PbSe and PbTe are estimated to be 23 and 70 nm, respectively,[2] which are significantly larger than those for II-VI semiconductors such as CdSe ($a_e \sim 3$ nm and $a_h \sim 1$ nm).[3] The materials are technologically interesting because the absence of a degenerate heavy hole band reduces nonradiative Auger recombination rates by more than 1 order of magnitude as compared with III-V and II-VI materials that have similar narrow band gaps.[4] Moreover, unlike larger band gap II-VI materials, IV-VI QDs can be tuned with dot size to be optically active in the mid- and near-infrared spectral regions, so IV-VI QDs are promising materials for novel infrared-optical devices including optoelectronic components for 1.3 and 1.55 μm fiber optical communications.[5]

IV-VI QDs have been fabricated by molecular beam epitaxy and other synthesis methods.[2,6–8] Recently, Heiss *et al.*[9] demonstrated that PbTe QDs could be fabricated by annealing PbTe(001)/CdTe(001) single quantum well structures at different temperatures and observed room-temperature midinfrared photoluminescence with intensities significantly higher than those observed from their best PbTe bulk or quantum well samples. Transmission electron microscopy characterization showed that the PbTe/CdTe QDs had a highly symmetric geometry of a small-rhombo-cubo-octahedron with three interface classes {100}, {110}, and {111} around the periphery of the dots [see Fig. 1(a)].[9] These QD geometries are quite different from the spherical one that was modeled in previous analysis of IV-VI QDs.[10,11] In addition, the quantum confinement potential in the PbTe/CdTe QDs is much smaller ($\Delta E_g = 1.2$ eV) than the IV-VI/SiO$_2$ QDs modeled in prior work, so a finite potential well model is needed instead of the infinite potential well model used earlier,[10,11] where the high order $o(k_i^4)$ contribution to the Hamiltonian was not considered. Furthermore, the newly realized PbTe/CdTe QDs[9] had dot sizes much bigger, on the order of 25 nm, than those modeled previously. In this paper, we present a theoretical model to calculate interband optical transitions in PbTe/CdTe zero dimensional structures in which two types of QDs are involved, cubic and elongated ones. The QD geometry is approximated by a quantum box with six {100} facets. The model is based on the four-band $\vec{k}\cdot\vec{p}$ envelope function approach, which takes into account the anisotropic effects of the band structure of the IV-VI semiconductors (the constant energy surfaces are prolate ellipsoids of revolution characterized by longitudinal and transverse effective masses, $m_{\parallel}^*$ and $m_{\perp}^*$, respectively, with the major axes of the ellipsoids in the $\langle 111 \rangle$ directions) and the finite-confinement-potential effect. The high order $o(k_i^4)$ contribution to the Hamiltonian is also calculated using the perturbation approximation. Using the model, we successfully describe the observed photoluminescence (PL) spectra from high-symmetry PbTe quantum dots embedded in (001)-oriented CdTe matrix material.[9] This theoretical model can be extended to interpret also the interband optical transitions in other IV-VI QDs, such as PbSe/PbTe and PbSe/PbEuTe
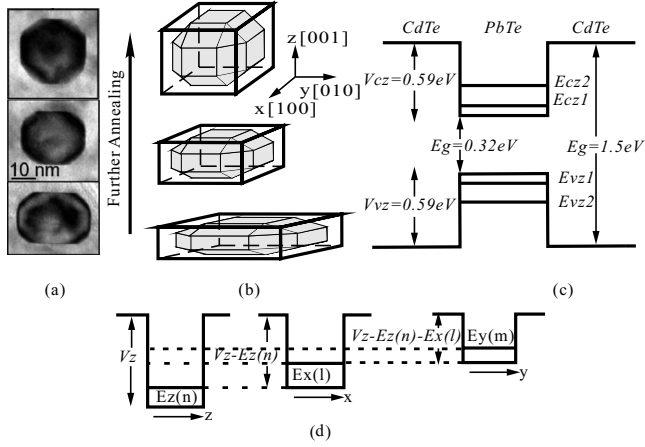
FIG. 1. The description of PbTe/CdTe QD heterosystem: (a) cross sectional TEM images of PbTe/CdTe QDs derived from Ref. 9, (b) geometry evolution of a PbTe QD versus annealing temperatures and quantum box approximations, (c) the band alignment of PbTe/CdTe heterosystem, (d) the three-dimensional (3D) potential well of a quantum box is decomposed into three one-dimensional (1D) wells that lie along the *x*, *y*, and *z* directions.

QDs[6] that have a small confinement potential and are oriented in different directions ([001], [111], or [110]) by appropriate projection of a coordinate axis.

The paper is organized as follows. In Sec. II, we present system descriptions and anisotropic calculations for PbTe/CdTe QDs. In Sec. III, we present the model to calculate spontaneous emission rates in PbTe/CdTe QDs. In Sec. IV, we show the calculated results of interband transition energies and emission spectra of PbTe/CdTe QDs with uniform dot size. Also, we show the simulation results of photoluminescence spectra of QD ensembles, and the validity and utility of the model are discussed. Finally, in Sec. V, we present the conclusions of this paper.

II. SYSTEM DESCRIPTIONS AND ANISOTROPY CALCULATIONS

The morphologies and energy levels for PbTe(001)/CdTe(001) QDs are shown in Fig. 1. As characterized by transmission electron microscopy (TEM),[9] after thermal annealing at 250 °C, the PbTe/CdTe quantum well structure was firstly broken up into elongated islands with an average thickness of about 10 nm and lateral extents of several 100 nm. These elongated islands were then partially transformed into highly symmetric QDs with an average size of about 25 nm after further annealing at a temperature higher than 280 °C. The QDs exhibit symmetric geometry with {100}, {110}, and {111} facets, a geometric shape of small-rhombo-cubo-octahedrons, as sketched in Fig. 1(b) with gray color. This PbTe QD geometry results from the exposure of the low surface energy crystallographic planes as the system approaches thermodynamic equilibrium at high annealing temperatures.[9] To calculate the band energies and optical transitions in these interesting QDs, the highly symmetric QD is approximated by a cubic quantum box with

{100} facets and the elongated island is approximated by a compressed quantum box with an average height of 10 nm. Type I band alignment was assumed for the PbTe/CdTe interface,[12] as shown in Fig. 1(c). It is assumed here that the ratio between the conduction and the valence band offsets $(\Delta E_c/\Delta E_v)$ is 1:1 due to the high symmetry of conduction band and valence band and the lack of reliable data on band offsets at the PbTe/CdTe heterointerface. To verify this assumption, we calculated the transition energies of ground states at different band offsets $(\Delta E_c/\Delta E_v=1:1, 4:1,$ and $11:1)$ and found that for PbTe QDs with dot size larger than 20 nm, the band offset variation only leads to a small change of the interband transition energies (<15 meV). The band gap of PbTe is 0.32 eV at 300 K,[13] and that of CdTe is 1.5 eV.[14] The three-dimensional (3D) potential well of the quantum box can be decomposed into three one-dimensional (1D) wells that lie along the *x*, *y*, and *z* directions.[15] These 1D potential wells are plotted in Fig. 1(d).

As mentioned above, the IV-VI semiconductors have anisotropic band structure characteristics. The anisotropy of the constant energy surfaces can be taken into account through calculations of quantized energy levels in QDs (see Appendix A). The so-called carrier mobility effective masses m_w^* $=3m_\perp^* m_\parallel^*/(2m_\parallel^*+m_\perp^*)$ in Eq. (A11) for (001)-oriented PbTe/CdTe QDs are the same to those in the [001] confined direction of IV-VI QWs, which were derived from the energy dispersion relations for IV-VI semiconductors using Kane's two-band model.[16] Using the longitudinal and transverse effective masses, $m_\parallel^*$ and $m_\perp^*$ at 300 K,[17] the mobility effective masses of the PbTe QDs are calculated to be $m_{ew}^*=0.043m_0$ for electrons and $m_{hw}^*=0.050m_0$ for holes. The electron and hole effective masses of the CdTe matrix material are isotropic and the values are $m_e^*=0.11m_0$ and $m_h^*=0.35m_0$, respectively.[18]

III. CALCULATION OF SPONTANEOUS EMISSION RATE

The spontaneous emission from a PbTe QD originates from the interband recombination of an electron with a hole in discrete energy levels, and the excitonic effect can be neglected due to the extremely high dielectric constant of ~400 for bulk PbTe.[19] The calculation of discrete energy levels and envelope wave functions for (001)-oriented PbTe QDs is given in Appendix A and the calculation of the optical transition matrix elements is given in Appendix B. The optical gain for semiconductor QDs is given in Ref. 20, and the spontaneous emission rate for PbTe QDs can be expressed by

$$R_{sp}(E) = \frac{8\pi n_r^2 E^2}{h^3 c^2} \frac{f_c(1-f_v)}{f_c-f_v} g(E)$$

$$= \frac{8\pi n_r N_D e^2 E^2}{h^2 c^3 \varepsilon_0 m_0^2} \sum_{c,v} \frac{|P_{cv}^\sigma|^2}{E_{cv}} f_c(1-f_v) B_{cv}(E-E_{cv}),$$

(1)

where f_c is the electron probability distribution function in the conduction band, f_v is the hole probability distribution function in the valence band, N_D is the volume density of dots, n_r is the refractive index, and E_{cv} is the interband tran-

sition energy, $E_{cv}=E_g+E_c+E_v$. Formula (1) takes homogeneous broadening into consideration, which has a Lorentzian shape as

$$B_{cv}(E - E_{cv}) = \frac{\hbar\Gamma_{cv}/\pi}{(E - E_{cv})^2 + (\hbar\Gamma_{cv})^2}, \qquad (2)$$

where Γ_{cv} is the polarization dephasing or scattering rate.[20] The carrier probability distribution functions (f_c, f_v) are related to the carrier density,

$$N = \sum_{lmn} \frac{2\delta(E_c - E_{clmn})}{V} f_c(E_c)$$

$$= \sum_{lmn} \frac{2}{\left[1 + \exp\left(\dfrac{E_{clmn} - E_{fc}}{kT}\right)\right]w_x w_y w_z}, \qquad (3)$$

$$P = \sum_{lmn} \frac{2\delta(E_v - E_{vlmn})}{V} f_v(E_v)$$

$$= \sum_{lmn} \frac{2}{\left[1 + \exp\left(\dfrac{E_{fv} - E_{vlmn}}{kT}\right)\right]w_x w_y w_z}, \qquad (4)$$

where N and P represent the electron and hole densities, respectively. The quasi-Fermi energy levels (E_{fc}, E_{fv}) and discrete energy levels (E_{clmn}, E_{vlmn}) are measured from band edges into bands for $E_{fc}, E_{clmn} > 0$ and $E_{fv}, E_{vlmn} > 0$. w_x, w_y, and w_z are the widths of the QDs along the x, y, and z directions, respectively.

The spontaneous emission spectra of the PbTe/CdTe QDs are calculated by using the above theoretical model. The parameters used in the calculations are as follows. The refractive index (n_r) for PbTe is 5.5. The dot density (N_D) is assumed to be the same value for all QDs with different sizes. As a result, the calculations give comparable emission intensities for different types of QDs. $\hbar\Gamma_{cv}=10$ meV is assumed at 300 K, as given in Ref. 20. For the calculation of the transition matrix element of Eq. (B8), we use $E_g=0.32$ eV, $m_\perp=m_{e\perp}^*$, and $m_\parallel=m_{e\parallel}^*$.

IV. RESULTS AND DISCUSSION

A. Spontaneous emission spectra of the PbTe/CdTe quantum dots with uniform dot size

As a first step, we have calculated interband transition energies for PbTe(001)/CdTe(001) QDs with a uniform dot size by using the approximation of Appendix A. The high order term of the Hamiltonian in Eq. (A11), $o'(k_i^4)$, is treated by the perturbation approach. Figure 2 shows the ground state (1-1) and the first excited state (2-2) transition energies as a function of dot size. The ground state transition energy is 855 meV for 5 nm QDs. It sharply decreases to 376 meV as the dot size increases to 25 nm and then decreases slowly to 336 meV as the dot size reaches 50 nm. For comparison, the transition energies of elongated islands with a height of 10 nm and the lateral extents of 30–50 nm are also plotted in
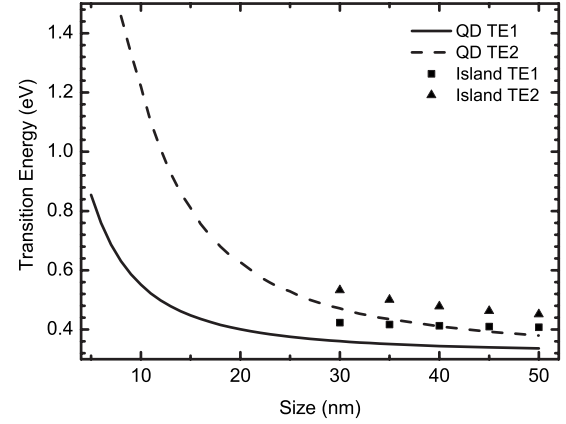

FIG. 2. The calculated transition energies for PbTe QDs as a function of dot size. The solid line is for the ground state (1-1) interband transitions in the QDs. The dashed line is for the first excited state (2-2) interband transitions in the QDs. The squares and triangles are for the (1-1) and (2-2) transitions in the elongated islands, respectively.

Fig. 2. The transition energies of the elongated islands are higher than those of the QDs due to stronger quantum confinement in the vertical direction (along the z axis). It can be seen in Fig. 2 that in the dot size region of 30–50 nm, the difference of the ground state transition energies between the QDs and elongated islands is about 69 meV.

The quasi-Fermi energy in the conduction band (E_{fc}) as a function of electron density is plotted in Fig. 3 with the dot size as a parameter. The quasi-Fermi energies for dots and islands are almost the same and overlapped with each other, and they increase with the electron density. The E_{fc} of the PbTe bulk material[21] is also plotted in Fig. 3 for comparison. At a fixed electron density, the E_{fc} of PbTe QDs is much higher than that of bulk PbTe. The difference of E_{fc} between the low-dimensional structures and the bulk material enlarges with the increase of injected electron density.

Figure 4(a) shows the calculated spontaneous emission spectra of the PbTe QDs as a function of dot size at an
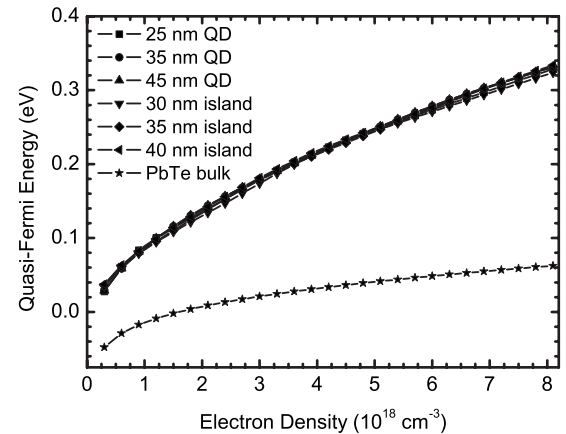

FIG. 3. The quasi-Fermi energies as a function of electron density for PbTe QDs and elongated islands. The quasi-Fermi energies of PbTe bulk (labeled by stars) are also plotted for comparison.
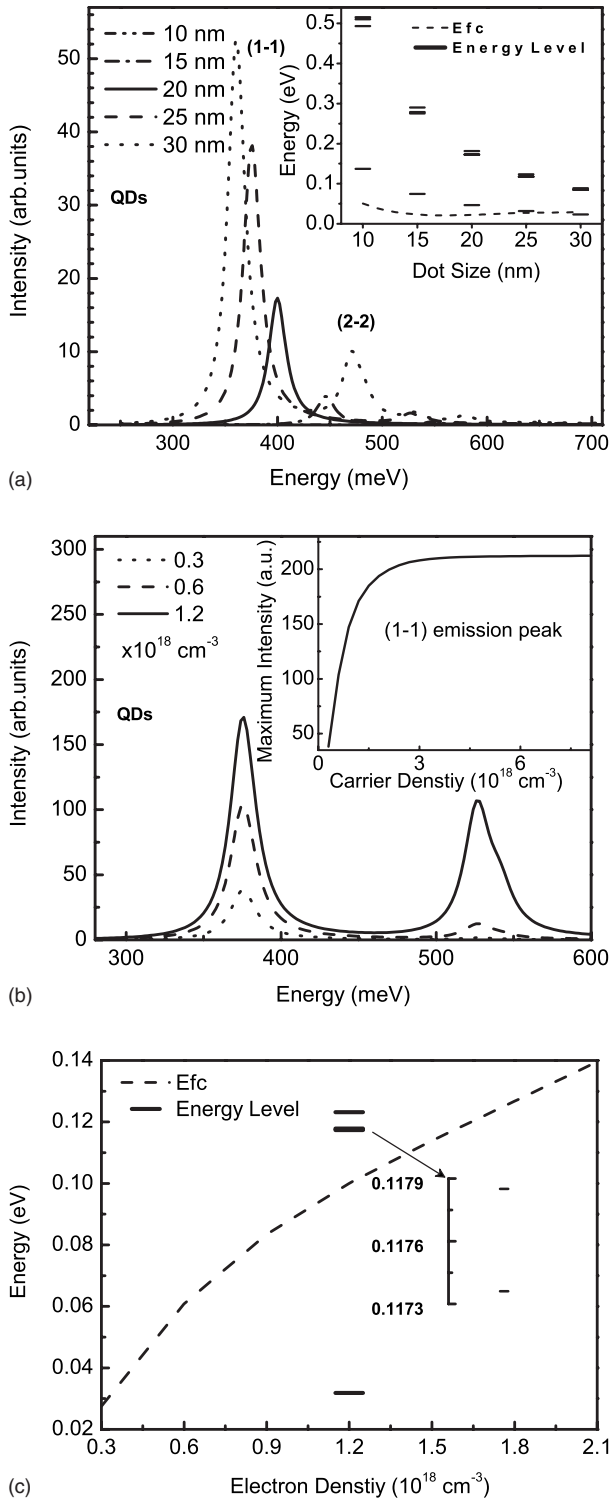
(a)

(b)

(c)

FIG. 4. (a) The calculated spontaneous emission spectra of PbTe QDs at different dot sizes with an injected carrier density of 3×10^{17} cm^{-3}. The inset shows the dependence of discrete energy levels and quasi-Fermi energies on the dot size. (b) The calculated spontaneous emission spectra of the PbTe QDs (size: 25 nm) at different carrier densities. The inset shows the maximum emission intensity of the ground state (1-1) transition at different carrier densities, and it saturates at the carrier density of 3×10^{18} cm^{-3}. (c) The quasi-Fermi energies vs carrier density for a 25 nm QD. The ground and the first excited energy levels are also shown.

injected carrier density of 3×10^{17} cm^{-3}. It can be seen that the emissions from 10 and 15 nm QDs are weak and are located at 548 and 446 meV, respectively. These emissions originate from the recombination of electrons and holes in the ground states (1-1). As the dot size increases, the peak intensity of the (1-1) transition gets stronger and the emission from the first excited states (2-2) emerges when the dot size is larger than 20 nm. The reason for this behavior is that the QD energy levels shift down to the extrema of the bands as the dot size increases and below the quasi-Fermi energy level, which is shown in the inset of Fig. 4(a). As a result, the product $f_c(1-f_v)$ increases with the dot size, and that leads to higher spontaneous emission rates. For a QD with typical size of 25 nm, as an example, the emission is a function of carrier density.

Figure 4(b) shows that at high-injected carrier densities, the emission intensity from the first excited state increases more quickly than that from the ground state. This can be attributed to the ground state being fully occupied at high-injected carrier densities (E_{fc} is higher than the ground energy level), and then the emission intensity reaches saturation. The peak intensity of the (1-1) transition saturates at 3×10^{18} cm^{-3}, as shown in the inset of Fig. 4(b). Another factor is that the first excited state is twofold degenerate in a QD, as given in Fig. 4(c). Consequently, more electrons are needed to fill the first excited state energy level. This result indicates that the emission spectra of PbTe QDs will change at different pumping powers, which has already been observed by PL measurements of PbTe/CdTe QDs.[9] It should be emphasized that this effect, caused by the different state degeneracies that are particular to IV-VI semiconductors, has not been investigated in prior work.

The calculated spontaneous emission spectra of the elongated islands at an injected electron density of 3×10^{17} cm^{-3} are given in Fig. 5. Figure 5(a) displays the calculated spontaneous emission spectra of the PbTe elongated islands at different lateral sizes but with a fixed height of 10 nm. Figure 5(b) shows the calculated spontaneous emission spectra of PbTe elongated islands at different heights but with a fixed lateral size of 40 nm. The peak intensities of the (2-2) transition are comparable to those of the (1-1) transition. The change of the (1-1) peak positions versus island height is more pronounced than those with different lateral sizes. Moreover, peak shifts decrease as the island size increases. For example, a redshift of ~4 meV for the (1-1) peak is observed as the lateral size increases from 40 to 45 nm, and so is that of ~2 meV as the lateral size increases from 45 to 50 nm. Compared to the QDs that have a size larger than 25 nm, the elongated islands of interest in this work show weaker (1-1) emission intensities. This is because the islands have almost the same quasi-Fermi energy level but higher ground energy levels, as compared with the QDs. Consequently, the occupation probability of the ground state in elongated islands is smaller than that in QDs.

B. Simulation of photoluminescence spectra and dot size distributions of the PbTe/CdTe quantum dot ensembles

The above calculations of the spontaneous emission spectra of PbTe/CdTe QDs with a uniform dot size can be used
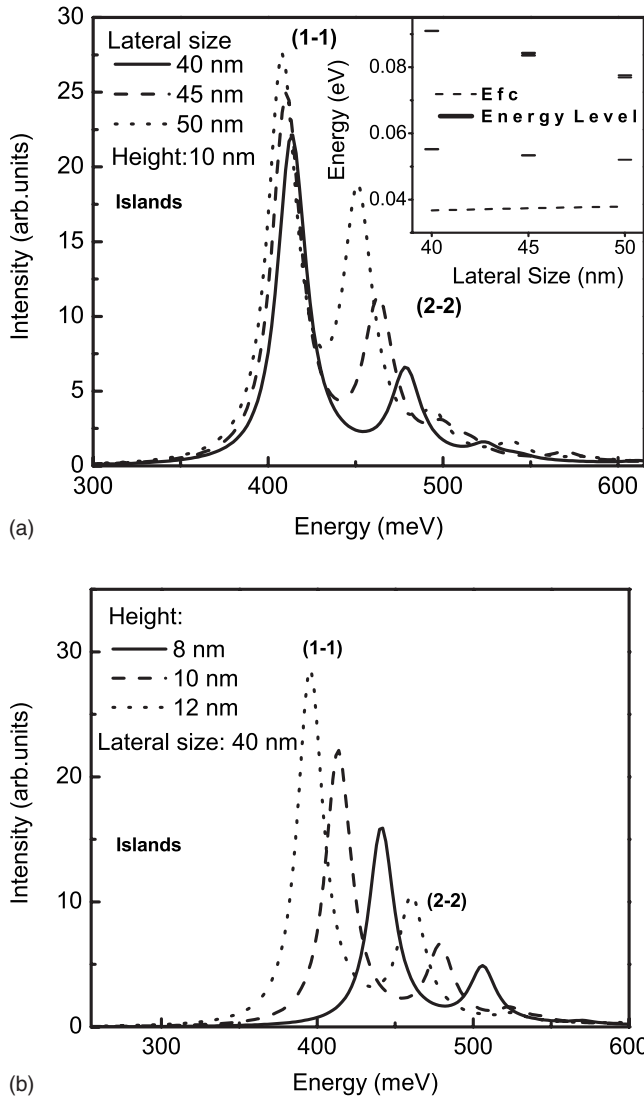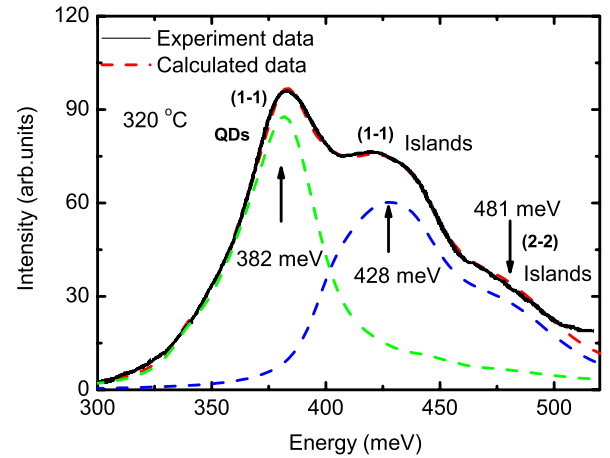
FIG. 6. (Color online) Measured photoluminescence spectra (solid line) and the simulated results (dashed line) for PbTe/CdTe heterostructure [the sample was annealed at 320 °C (Ref. 9)].

fluctuations has been included in the spontaneous emission formula [Eq. (1)] by defining a weight function $W(x)$ as follows:

$$R_{SP} = \sum_{x} W(x) r_{sp}(x), \qquad (5)$$

where R_{SP} is the photoluminescence spectrum from the ensemble of dots and $r_{sp}(x)$ is the spontaneous emission spectrum from dots with the single size of x. $W(x)$ is the weight distribution function of dots with the size of x to the PL spectrum, an exclusive fitting parameter. The relative dot size distribution can be evaluated by $W(x)/\Sigma_x W(x)$.

The measured and simulated PL spectra are plotted in Fig. 6. It can be seen that the calculated lines are in good agreement with the experimental data. From the simulated results, it can be concluded that the broad PL spectrum is composed of two quantum structures: the emission at about 382 meV (3.2 μm) from the ground state transition of the high-symmetry quantum dot ensemble and the emissions at 428 meV (2.9 μm) and 481 (2.6 μm) meV from the ground and the first excited state transitions of the elongated islands, respectively. The relative size distributions for QDs and for elongated islands are shown in Fig. 7. It can be seen from Fig. 7 that the central distribution of the quantum dots for the sample annealed at 320 °C is at 23 nm. For the samples annealed at 280 and 250 °C, the simulation results show that the central distribution of the quantum dots is at 21 nm. Figure 7 gives the central distribution of the elongated islands as well at the height of 8 nm. The calculated dot sizes are in good agreement with those measured by TEM with a small error range ($\sim$2 nm). The size deviation of the calculations from the measured one can arise from the difference between the shape of small-rhombo-cubo-octahedrons (observed by TEM) and the cuboid geometries used in our model. The volume of a cube is slightly larger than that of rhombo-cubo-octahedron that is inscribed in the cube by cutting the vertices. Therefore, the quantum confinement in the experimentally realized PbTe/CdTe QDs is underestimated in some

FIG. 5. (a) Calculated spontaneous emission spectra of PbTe elongated islands at different lateral sizes. The height of the islands is fixed at 10 nm. The inset shows the dependence of discrete energy levels and quasi-Fermi energies on the lateral size of islands. (b) Calculated spontaneous emission spectra of PbTe elongated islands at different heights. The lateral size of islands is fixed at 40 nm.

to simulate the PL spectra measured from PbTe/CdTe QD ensembles by which one can obtain the dot size distribution of the PbTe/CdTe heterosystem. By comparing the calculated dot size distribution with that measured from TEM in Ref. 9, we can proof test the validity and utility of our theoretical model.

The experimental data to be simulated here are photoluminescence spectra that are derived from Ref. 9. By characterization with TEM, two types of PbTe low-dimensional structures were observed in the PbTe/CdTe heterosystem, i.e., the highly symmetric quantum dots with an average size of 25 nm and the elongated islands with a height of about 10 nm. Therefore, the calculation of optical transitions should include these two types of low-dimensional structures. Inhomogeneous broadening due to dot size distribution
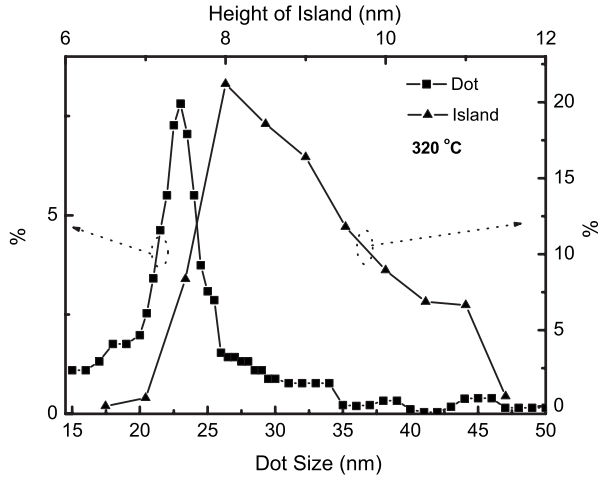
FIG. 7. Calculated dot size distribution of the PbTe QDs and height distribution of the PbTe elongated islands in the PbTe/CdTe heterostructure annealed at 320 °C.

sort by our cuboid-geometry approximation. The dot sizes derived from the simulations are, therefore, slightly smaller than the sizes measured by TEM. However, this small deviation can be easily calibrated by taking into account the geometric shape difference.

Further simulations of the PL spectra measured from other QD samples that were fabricated by different annealing temperatures (250 and 280 °C) in Ref. 9 indicate that the dot size distribution varies rarely with annealing temperature. This result may explain the absence of PL peak shift of the samples after different annealing temperatures. However, the comparison of emission peak intensities of the QDs and elongated islands indicates that the percent ratio of QD number to that of elongated islands varies with annealing temperature, from 33% for 250 °C, 50% for 280 °C, to 80% for 320 °C. This means that more elongated islands were transformed into quantum dots as the annealing temperature was increased. As a result, the PL emission from the QD ensemble exceeds that from elongated islands after annealing at a higher temperature.

V. SUMMARY AND CONCLUSIONS

To describe the interband transitions of PbTe QDs embedded in a CdTe single crystalline matrix, we have developed a theoretical model that accounts for the anisotropy of the PbTe band structure and the finite-confinement potential of PbTe/CdTe heterosystem. Using the model, we have calculated the spontaneous emission spectra of the ground and the first excited state transitions of PbTe QDs with different dot sizes and injected carrier densities. The simulation of the measured photoluminescence spectra for the PbTe/CdTe heterostructure indicates the existence of the two types of quantum structures created by thermal annealing of the PbTe/CdTe quantum wells grown by MBE, i.e., highly symmetric quantum dots and elongated islands. The calculations of the size distribution for PbTe QDs are in good agreement with the TEM observation shown in Ref. 9, which verifies

the validity of the model in the description of an actual IV-VI QD system that has different dot orientations, finite-confinement potential, and anisotropic bands. The good description of spontaneous emission spectra for PbTe/CdTe QDs by this model shows that it can be readily applied to the design and fabrication of midinfrared optoelectronic devices such as PbTe/CdTe QD laser diodes and detectors. Furthermore, it is possible to extend this model to the description of optical transition in other IV-VI QDs, such as PbSe/PbTe and PbSe/PbEuTe QDs that are large pyramids (with a typical lateral size of 50 nm and height of 20 nm) oriented in different directions and having small quantum confinement potential ($<$100 meV).

APPENDIX A: THE ANISOTROPIC FOUR-BAND ENVELOPE-FUNCTION APPROXIMATION

To calculate the energy levels and the wave functions for electrons and holes in cuboid-geometry QDs, we used a four-band model, which takes into account the anisotropy and accurately describes the band structure near the L point of bulk PbTe. For IV-VI bulk materials, the conduction-band edge is p-like, which is doubly degenerate having the Bloch spin-orbital pair $L_6^-\uparrow(\vec{r},\sigma)$ and $L_6^-\downarrow(\vec{r},\sigma)$ due to the crystal field and spin-orbit interaction. The valence-band edge is s-like, which is doubly degenerate due to spin, with the Bloch spin-orbital pair $L_6^+\uparrow(\vec{r},\sigma)$ and $L_6^+\downarrow(\vec{r},\sigma)$.[22] Away from the L point, the wave functions are sums of products of the Bloch functions at the band-edge point of the Brillouin zone and slowly varying envelope functions $f_i(\vec{r})$,

$$\psi(\vec{r},\sigma) = f_1(\vec{r})L_6^-\uparrow(\vec{r},\sigma) + f_2(\vec{r})L_6^-\downarrow(\vec{r},\sigma)$$
$$+ f_3(\vec{r})L_6^+\uparrow(\vec{r},\sigma) + f_4(\vec{r})L_6^+\downarrow(\vec{r},\sigma). \quad (A1)$$

The envelope functions obey the following equation:

$$\begin{pmatrix} H_- & 0 & \frac{\hbar}{m_0}P_\parallel k_z & \frac{\hbar}{m_0}P_\perp k_- \\ 0 & H_- & \frac{\hbar}{m_0}P_\perp k_+ & -\frac{\hbar}{m_0}P_\parallel k_z \\ \frac{\hbar}{m_0}P_\parallel k_z & \frac{\hbar}{m_0}P_\perp k_- & H_+ & 0 \\ \frac{\hbar}{m_0}P_\perp k_+ & -\frac{\hbar}{m_0}P_\parallel k_z & 0 & H_+ \end{pmatrix} \begin{pmatrix} f_1 \\ f_2 \\ f_3 \\ f_4 \end{pmatrix}$$
$$= E \begin{pmatrix} f_1 \\ f_2 \\ f_3 \\ f_4 \end{pmatrix}, \quad (A2)$$

where $H_\pm = \mp[E_g/2 + (1/2m_t^\pm)k_t^2 + (1/2m_l^\pm)k_z^2]$, E_g is the band

gap, $P_\parallel$ and $P_\perp$ are the longitudinal (along [111]) and perpendicular momentum interband matrix elements, $m_l^\pm(m_t^\pm)$ are the far band contributions to the longitudinal (transverse) band-edge effective masses, $k_t^2 = k_x^2 + k_y^2$, $k_z = -i\partial/\partial z$, and $k_\pm = k_x \pm i k_y = -i(\partial/\partial x \pm i\partial/\partial y)$. In this four-band $\vec{k}\cdot\vec{p}$ model, the anisotropic effects of the band structure are included in the off-diagonal elements.

For IV-VI bulk material, the envelope functions are plane waves $\exp(i\vec{k}\cdot\vec{r})$ and the eigenvalues E are the energy-band dispersion functions $E(\vec{k})$. However, for quantum confined structures such as quantum dots, the appropriate boundary conditions at the interfaces should be taken into account, and the envelope functions are no longer plane waves but the solution of four coupled second-order differential equations. These equations have been used to investigate the nonparabolic and anisotropic quantized states for one-dimensional confinement structure (PbTe QWs) in which $H_\pm = \mp E_g/2$ and two different sets of effective momentum matrix elements $\{P_\parallel^e, P_\perp^e\}$ and $\{P_\parallel^h, P_\perp^h\}$ are used to calculate independently the quantized state energies of an electron and a hole.[23] The present work extends the model of Ref. 23 to calculate electron energy levels in IV-VI quantum dots. Equation (A2) can be rewritten as

$$\begin{pmatrix} h_c & h_{cv} \\ h_{vc} & h_v \end{pmatrix} \begin{pmatrix} f_c \\ f_v \end{pmatrix} = E \begin{pmatrix} f_c \\ f_v \end{pmatrix}, \qquad \text{(A3)}$$

where h_c, h_v, and $h_{cv} = h_{vc}$ are 2×2 matrix operators. After a simple algebra, one can obtain

$$H_{2\times2}^c f_c = [h_c + h_{cv}(E - h_v)^{-1} h_{vc}] f_c = E f_c, \qquad \text{(A4a)}$$

$$H_{2\times2}^v f_v = [h_v + h_{vc}(E - h_c)^{-1} h_{cv}] f_v = E f_v. \qquad \text{(A4b)}$$

For the longitudinal valley in a IV-VI QD grown along the [111] direction, the coordinate frame system is set as $x \| [1\bar{1}0], y \| [11\bar{2}]$, and $z \| [111]$, and $h_c = [H_- + Q(x,y,z)]I$ and $h_v = [H_+ + Q(x,y,z)]I$, where I is the 2×2 unit matrix and $Q(x,y,z)$ is a step function that sets the position of the center of the gap along the confined direction. Performing now the matrix products in Eq. (A4a), for example, we get the following effective Hamiltonian for the conduction band:

$$H_{2\times2}^{cL} = \left(-\frac{\hbar^2}{2}\frac{\partial}{\partial z}\frac{1}{m_\parallel}\frac{\partial}{\partial z} - \frac{\hbar^2}{2}\frac{\partial}{\partial x}\frac{1}{m_\perp}\frac{\partial}{\partial x} \right.$$
$$\left. -\frac{\hbar^2}{2}\frac{\partial}{\partial y}\frac{1}{m_\perp}\frac{\partial}{\partial y} + \frac{E_g}{2} + Q \right) I + \vec{\alpha}_{so} \cdot (\vec{\sigma} \times \vec{K}) + o(k_i^4),$$
$$\text{(A5)}$$

where

$$m_{\parallel,\perp} = m_{\parallel,\perp}(x,y,z,E) = \frac{1}{2\left(\dfrac{P_{\parallel,\perp}^2}{A m_0^2} + \dfrac{1}{2 m_{l,t}^-} \right)},$$

$$A = \left[E + \frac{E_g(x,y,z)}{2} - Q(x,y,z) \right], \qquad \text{(A6)}$$

$$\vec{\alpha}_{so} = \frac{\hbar}{m_0}\left(P_\perp \frac{\partial}{\partial x}\frac{1}{A}, P_\perp \frac{\partial}{\partial y}\frac{1}{A}, P_\parallel \frac{\partial}{\partial z}\frac{1}{A} \right), \qquad \text{(A7)}$$

$$\vec{K} = \frac{\hbar}{m_0}(P_\perp k_x, P_\perp k_y, P_\parallel k_z). \qquad \text{(A8)}$$

Here, $\vec{\sigma}$ is the vector of the Pauli spin matrices. The second term in Eq. (A5) is the so-called Rashba spin-orbit term $[\vec{\alpha}_{so} \cdot (\vec{\sigma} \times \vec{K})]$. Note that this term is zero for $\vec{K} = 0$ and $E_g(x,y,z)$ and $Q(x,y,z)$ are constant in QD and barrier material. Therefore, in our case, the Rashba spin-orbit term is not considered because a cuboid quantum box has a symmetric geometry. The last term, $o(k_i^4)$, is a 2×2 matrix of $k_i^4(i = x, y, z)$, which is a small quantity (especially for large quantum dots and for optical transitions close to the band edge) and can be treated by the perturbation theory. It is worth noting that the anisotropic effects of the band structure are presented in the effective masses $m_{\parallel,\perp}$.

The quantized energy levels in cuboid QDs are spin degenerate and satisfy the following Schrödinger-like equation:

$$H_c^L(E_{clmn}^L)f_{clmn} = \left[-\frac{\hbar^2}{2}\frac{\partial}{\partial z}\frac{1}{m_\parallel}\frac{\partial}{\partial z} - \frac{\hbar^2}{2}\frac{\partial}{\partial x}\frac{1}{m_\perp}\frac{\partial}{\partial x} - \frac{\hbar^2}{2}\frac{\partial}{\partial y}\frac{1}{m_\perp}\frac{\partial}{\partial y} \right.$$
$$\left. + V(x,y,z) + o(k_i^4) \right] f_{clmn} = E_{clmn}^L f_{clmn}, \qquad \text{(A9)}$$

where $V(x,y,z) = E_c(x,y,z) = E_g(x,y,z)/2 + Q(x,y,z)$ gives then the conduction-band edge modulation along the confined direction and E_{clmn}^L are the longitudinal valley subbands.

For IV-VI QD grown along the [001] direction, all four energy valleys are oblique and degenerate. The subbands in oblique valleys can be obtained after an appropriate rotation of the coordinate axis. To calculate electron states in oblique valley along the [111] direction, as an example, we take z [001] as the first rotation axis and perform the rotation with an angle of $\alpha = \pi/4$, get a new coordinate frame system as $(x' \| [1\bar{1}0], y' \| [110], z' \| [001])$, then take x' as the second rotation axis and perform the rotation with angle of $\beta = \arccos(\frac{1}{\sqrt{3}})$, and get a double primed coordinate frame system as $(x'' \| [1\bar{1}0], y'' \| [11\bar{2}], z'' \| [111])$. The effect of the two rotations on the Hamiltonian can be obtained by calculating $H_{2\times2}^O = T_\beta T_\alpha H_{2\times2}^L T_\alpha^{-1} T_\beta^{-1}$ with

$$T_\gamma = \begin{pmatrix} \cos\left(\dfrac{\gamma}{2}\right) & i\sin\left(\dfrac{\gamma}{2}\right) \\ i\sin\left(\dfrac{\gamma}{2}\right) & \cos\left(\dfrac{\gamma}{2}\right) \end{pmatrix}, \quad \gamma = \alpha, \beta. \qquad \text{(A10)}$$

Substituting $\vec{k} = (k_x, k_y, k_z)$ by $\vec{k}'' = (k_x/\sqrt{2} - k_y/\sqrt{2}, k_x/\sqrt{6} + k_y/\sqrt{6} - \sqrt{2/3}k_z, k_x/\sqrt{3} + k_y/\sqrt{3} + k_z/\sqrt{3})$, then one can write

$$H_c^O(E_{clmn}^O) = -\frac{\hbar^2}{2}\frac{\partial}{\partial z}\frac{1}{m_1}\frac{\partial}{\partial z} - \frac{\hbar^2}{2}\frac{\partial}{\partial x}\frac{1}{m_2}\frac{\partial}{\partial x}$$

$$-\frac{\hbar^2}{2}\frac{\partial}{\partial y}\frac{1}{m_3}\frac{\partial}{\partial y} + V(x,y,z) + o'(k_i^4), \quad (A11)$$

where $m_{1,2,3} = m_w = 3m_\parallel m_\perp/(2m_\parallel + m_\perp)$ corresponds to the so-called mobility effective masses. The last term in Eq. (A11), $o'(k_i^4)$, being a 2×2 matrix of $k_i^4(i=x,y,z)$, is treated by the perturbation theory. It is obvious that one can apply a standard quantum mechanics methodology to obtain the solution for the quantized levels and envelope functions from Eq. (A11). The envelope functions take a sine or cosine wave form inside a cuboid dot and exponential decay functions outside the dot. The discrete energy levels (E_{xl}, E_{ym}, E_{zn}) of the cuboid QDs can be calculated with the potential $V(x,y,z)$ depicted in Fig. 1(d). The quantized energy levels of electrons in the PbTe QDs are obtained by

$$E_{clmn} = E_{xl} + E_{ym} + E_{zn}. \quad (A12)$$

The electron states in other oblique valleys for [111]-oriented QDs or for QDs with other orientation can also be calculated with Eq. (A11) by using the corresponding carrier mobility masses (m_1, m_2, m_3).

APPENDIX B: THE CALCULATIONS OF INTERBAND TRANSITION MATRIX ELEMENTS

The optical transition probability of an electron in a quantum box is proportional to the square of the interband transition matrix element, which can be expressed by

$$|P_{cv}^\sigma|^2 = |\langle \psi_{clmn}|\vec{e}\cdot\vec{p}_{cv}|\psi_{vlmn}\rangle|^2, \quad (B1)$$

where the subscript c (or v) denotes the conduction band (or valence band), l, m, and n denote the label of the quantized energy levels in the box, and ψ_{clmn} is the electron wave function that can be obtained from Appendix A.

It is noted that all four energy valleys of the IV-VI semiconductors are degenerate when quantization is in the [001] direction. Therefore, the four oblique valleys that are oriented along the [111], [$\bar{1}$11], [$1\bar{1}1$], and [$11\bar{1}$] directions have the same interband transition probability. The energy valley oriented along the z' axis parallel to [111] is shown in Fig. 8. The light is incident in the [001] direction with polarization vector $\vec{e}$ in the x,y plane of the unprimed coordinate frame (Fig. 8). The polarization vector has to be projected onto the primed coordinate axes because the basis functions $[L_6^-\uparrow(\vec{r},\sigma), L_6^-\downarrow(\vec{r},\sigma), L_6^+\uparrow(\vec{r},\sigma),$ and $L_6^+\downarrow(\vec{r},\sigma)]$ are correct only in the coordinate frame of the [111] valley (or the remaining valleys).[13] The polarization vector $\vec{e} = (\sin\varphi, \cos\varphi, 0)$ in the unprimed coordinate frame can be written as $\vec{e}' = [(\sin\varphi - \cos\varphi)/\sqrt{2}, (\sin\varphi + \cos\varphi)/\sqrt{6}, (\sin\varphi$
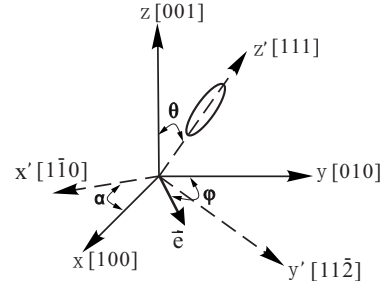

FIG. 8. The unprimed coordinate frame system is for a quantum box with {100} facets and the primed coordinate frame system is for the [111] constant-energy ellipsoid of PbTe near the L point of the Brillouin zone. The incident light is along the z direction and its polarization vector is denoted by $\vec{e}$, which is to be averaged over $0 \leq \varphi \leq 2\pi$ for unpolarized light.

$+\cos\varphi)/\sqrt{3}]$ in the primed coordinate frame. By using the set of matrix elements,[13,24]

$$\langle c\uparrow|\vec{e}'\cdot\vec{p}_{cv}(0)|v\uparrow\rangle = P_\parallel \vec{e}_z', \quad (B2)$$

$$\langle c\uparrow|\vec{e}'\cdot\vec{p}_{cv}(0)|v\downarrow\rangle = P_\perp(\vec{e}_x' + i\vec{e}_y'), \quad (B3)$$

$$\langle c\downarrow|\vec{e}'\cdot\vec{p}_{cv}(0)|v\uparrow\rangle = P_\perp(\vec{e}_x' - i\vec{e}_y'), \quad (B4)$$

$$\langle c\downarrow|\vec{e}'\cdot\vec{p}_{cv}(0)|v\downarrow\rangle = -P_\parallel \vec{e}_z', \quad (B5)$$

the interband transition matrix element for unpolarized light (averaged over all azimuth angles φ of the polarization vector $\vec{e}'$) is obtained by

$$|\langle c|\vec{e}\cdot\vec{p}_{cv}(0)|v\rangle|^2 = \sum_{i,j=\uparrow,\downarrow}^{oblique} |ci|\vec{e}\cdot\vec{p}_{cv}|vj|^2 = 2(2P_\perp^2 + P_\parallel^2)/3, \quad (B6)$$

where $P_\perp$ and $P_\parallel$ are the transverse and longitudinal momentum matrix elements and given as

$$\frac{2P_\perp^2}{m_0} = E_g\frac{m_0}{m_\perp}, \quad \frac{2P_\parallel^2}{m_0} = E_g\frac{m_0}{m_\parallel}, \quad (B7)$$

where $m_\perp$ and $m_\parallel$ are the anisotropic band-edge masses at the L point of the Brillouin zone.

Therefore, Eq. (B1) can be rewritten as

$$|P_{cv}^\sigma|^2 = |\langle f_{clmn}|f_{vlmn}\rangle|^2 |\langle c|\vec{e}\cdot\vec{p}_{cv}(0)|v\rangle|^2 = 2I_{cv}^2(2P_\perp^2 + P_\parallel^2)/3, \quad (B8)$$

where $I_{cv} = |\langle f_{clmn}|f_{vlmn}\rangle|$ is the overlap integral of the conduction- and valence-band envelope functions of QDs.

*hzwu@zju.edu.cn

[1] D. J. Mowbray and M. S. Skolnick, J. Phys. D **38**, 2059 (2005).

[2] A. Lipovskii, E. Kolobkova, V. Petrikov, I. Kang, A. Olkhovets, T. Krauss, M. Thomas, J. Silcox, F. Wise, Q. Shen, and S. Kycia, Appl. Phys. Lett. **71**, 3406 (1997).

[3] I. Kang and F. W. Wise, J. Opt. Soc. Am. B **14**, 1632 (1997).

[4] P. J. McCann, K. Namjou, and X. M. Fang, Appl. Phys. Lett. **75**, 3608 (1999).

[5] Z. Wu, Z. Mi, P. Bhattacharya, T. Zhu, and J. Xu, Appl. Phys. Lett. **90**, 171105 (2007).

[6] G. Springholz, V. Holy, M. Pinczolits, and G. Bauer, Science **282**, 734 (1998).

[7] K. Alchalabi, D. Zimin, G. Kostorz, and H. Zogg, Phys. Rev. Lett. **90**, 026104 (2003).

[8] E. Rodriguez, E. Jimenez, L. A. Padilha, A. A. R. Neves, G. J. Jacob, C. L. Cesar, and L. C. Barbosa, Appl. Phys. Lett. **86**, 113117 (2005).

[9] W. Heiss, H. Groiss, E. Kaufmann, G. Hesser, M. Boberl, G. Springholz, F. Schaffler, K. Koike, H. Harada, and M. Yano, Appl. Phys. Lett. **88**, 192109 (2006).

[10] A. D. Andreev, E. V. Kolobkova, and A. A. Lipovskii, J. Appl. Phys. **88**, 750 (2000).

[11] G. E. Tudury, M. V. Marquezini, L. G. Ferreira, L. C. Barbosa, and C. L. Cesar, Phys. Rev. B **62**, 7357 (2000).

[12] M. Yano, I. Makabe, and K. Koike, Physica E (Amsterdam) **20**, 449 (2004).

[13] Shu Yuan, H. Krenn, G. Springholz, and G. Bauer, Phys. Rev. B **47**, 7213 (1993).

[14] E. Matatagui, A. G. Thompson, and Manuel Cardona, Phys. Rev. **176**, 950 (1968).

[15] M. Asada, Y. Miyamoto, and Y. Suematsu, IEEE J. Quantum Electron. **QE-22**, 1915 (1986).

[16] M. F. Khodr, P. J. McCann, and B. A. Mason, IEEE J. Quantum Electron. **32**, 236 (1996).

[17] H. Preier, Appl. Phys. **20**, 189 (1979).

[18] Sotirios Baskoutas and Andreas F. Terzis, J. Appl. Phys. **99**, 013708 (2006).

[19] G. M. T. Foley and D. N. Langenberg, Phys. Rev. B **15**, 4830 (1977).

[20] M. Sugawara, K. Mukai, Y. Nakata, H. Ishikawa, and A. Sakamoto, Phys. Rev. B **61**, 7595 (2000).

[21] V. Altschul and E. Finkman, Appl. Phys. Lett. **58**, 942 (1991).

[22] R. Dalven, in *Solid State Physics: Advances in Research and Applications*, edited by F. Seitz, D. Turnbull, and H. Ehrenreich (Academic, New York, 1973), Vol. 28, p. 179.

[23] E. A. de Andrada e Silva, Phys. Rev. B **60**, 8859 (1999).

[24] D. L. Mitchell and R. F. Wallis, Phys. Rev. **151**, 581 (1966).